Mid-infrared Measurements of Ion-irradiated Carbonaceous Meteorites: How to Better Detect Space Weathering Effects

C. Lantz, T. Nakamura, D. Baklouti, R. Brunetto, E. Henault, S. Kobayashi, O. Mivumbi, Z. Djouadi, E. Quirico, M. Zolensky, et al.

The Planetary Science Journal, 5:201 (14pp), 2024 September https://doi.org/10.3847/PSJ/ad5d6f

Mid-infrared Measurements of Ion-irradiated Carbonaceous Meteorites: How to Better Detect Space Weathering Effects

C. Lantz[1,6], T. Nakamura[2], D. Baklouti[1], R. Brunetto[1], E. Henault[1], S. Kobayashi[2], O. Mivumbi[1], Z. Djouadi[1], E. Quirico[3], M. Zolensky[4], and T. Hiroi[5]
[1] Université Paris Saclay, CNRS, Institut d'Astrophysique Spatiale, 91405 Orsay, France
[2] Department of Earth Science, Tohoku University, Sendai 980-8578, Japan
[3] Université Grenoble Alpes, CNRS, Institut de Planétologie et d'Astrophysique de Grenoble, 38000 Grenoble, France
[4] NASA Johnson Space Center, Houston, TX 77058, USA
[5] Department of Earth, Environmental, and Planetary Sciences, Brown University, Providence, RI 02912, USA
Received 2023 October 17; revised 2024 June 17; accepted 2024 June 18; published 2024 September 17

Abstract

Remote sensing study of asteroids will soon enter a new era with an increasing amount of data available thanks to the JWST, especially in the mid-infrared (MIR) range that allows identification of mineral species. It will then be possible to establish a taxonomy, as is currently available in the visible–near-infrared range, based on MIR spectral parameters. It had been previously shown that the MIR range is very sensitive to space weathering (SpWe) effects. Thus, it is crucial to determine which spectral changes are involved to disentangle initial composition from surface aging and provide tools to interpret future remote sensing data of asteroids. We present here MIR measurements of a wide variety of ion-irradiated carbonaceous chondrites as a simulation of the solar wind SpWe component. We evaluate several parameters (the Christiansen feature and Reststrahlen band positions, the width of the main Si–O band) and test different measurement conditions (ion energy and geometry of observation). We highlight a dependency of the spectral changes with the initial composition, as hydrated samples are more affected than anhydrous ones. We confirm the role of the geometry in the detection of SpWe effects as already shown in the near-infrared, with a competition effect between the depth probed by photons and the implantation depth of ions (function of the energy used). We will discuss the results in the framework of future observations and Ryugu's and Bennu's samples studied in the laboratory.

Unified Astronomy Thesaurus concepts: Infrared spectroscopy (2285); Carbonaceous chondrites (200); Asteroid surfaces (2209)

1. Introduction

Space weathering (SpWe) is a general term used to describe the surface alteration processes of airless bodies in the solar system, in particular asteroids. Given the large compositional diversity of asteroids (DeMeo & Carry 2014), SpWe is not expected to produce the same effects on the different asteroid types.

SpWe effects on silicate-rich S-type asteroids have largely been investigated over the last decades (reviews by Clark et al. 2002 and Brunetto et al. 2015). Remote sensing observations on Eros and Itokawa (Clark et al. 2001; Hiroi et al. 2006; Ishiguro et al. 2007) together with spectral measurements on Itokawa returned grains (Bonal et al. 2015) confirmed the general trend of darkening and reddening (increasing slope toward longer wavelength) in the visible-to-near-infrared (VISNIR) range first observed on the Moon.

SpWe effects can be reproduced in the laboratory using ion (solar wind simulation) or laser (micrometeorite impact simulation) irradiation of analog samples. Numerous laboratory experiments on S-type analog materials, such as terrestrial silicates and ordinary chondrites, have been able to reproduce the products seen on the Itokawa samples: multilayered structures including amorphized silicates, nanophase reduced iron particles (npFe0), and iron sulfide inclusions (Noguchi et al. 2011, 2014).

Differently from S-types, there is no consensus on the spectral effects shown by C-complex asteroids when exposed to SpWe. Studies based on spectroscopic observations showed both reddening (Lazzarin et al. 2006; Fornasier et al. 2016; Kaluna et al. 2016) and blueing (Nesvorný et al. 2005; Lantz et al. 2013) effects on spectral slopes. Some discrepancy arose in the results of the laboratory experiments performed so far on C-type analogs (see Table 1 from Trang et al. 2021 for a list of experiments): anhydrous carbonaceous chondrites (CCs) show a red/dark trend, while hydrous CCs have various modifications in the VISNIR range. STEM analyses of irradiated laboratory analogs, such as CV Allende or CM Murchison (Matsuoka et al. 2015; Gillis-Davis et al. 2017; Thompson et al. 2019, 2020; Laczniak et al. 2021), highlighted the production of oxide and/or sulfide particles—different products than those seen for S-types.

Furthermore, a recent study using laser irradiation on a wide variety of meteorites (ordinary and enstatite chondrites, CCs, and aubrite) to cover the diversity of the asteroid population clearly points toward a nonuniversal model of SpWe (Zhang et al. 2022). The starting composition of exposed material thus plays a key role in the SpWe processes.

Another striking example of discrepancy among the C-type asteroids is when one compares Ryugu and Bennu. Both show signs of low reflectance and hydration, but the remote data point toward two SpWe regimes in the VISNIR.

[6] Corresponding author.

Hayabusa2/JAXA spectral data obtained with NIRS3 could not highlight a clear trend of SpWe at the surface of Ryugu regarding visible slope and reflectance value (Riu et al. 2021; Tatsumi et al. 2021). Still, based on ONC-T, there have been reports on the age–color relation on Ryugu: Sugita et al. (2019) showed that stratigraphically older units are redder and darker, and Morota et al. (2020) showed that this trend is consistent with solar heating or irradiation.

In contrast, Bennu materials observed by the OSIRIS-REx/NASA spacecraft apparently get bluer as a function of time (DellaGiustina et al. 2020; Lauretta et al. 2022).

The analysis on Earth of returned samples from Ryugu and Bennu is expected to reveal SpWe effects and, more generally, to elucidate the physicochemical modifications of C-type asteroids.

To better understand the discrepancy among CCs, some studies focused on irradiation of hydrated minerals (Kaluna et al. 2017; Rubino et al. 2020; Nakauchi et al. 2021) or SpWe products (Prince et al. 2020; Trang et al. 2021) commonly found in CCs. More parameters have been tested in recent years: the sample porosity and the energy used during irradiation have been shown to affect the spectral modifications in the VISNIR range (Nakamura et al. 2019; Matsuoka et al. 2020) and should be investigated further.

It remains crucial to look for more spectral indices that can be used, whatever the initial composition could be, and the VISNIR range has shown its limits. A few studies explored the whole IR range with the interesting conclusion that upon ion irradiation, all CCs (and common silicates) present a shift toward longer wavelengths of the main Reststrahlen bands (Vernazza et al. 2013; Lantz et al. 2017; Brunetto et al. 2018, 2020). This finding seems promising for using a reliable systematic tool for searching SpWe effects on large asteroid populations (e.g., with the instrument MIRI on board JWST; Rieke et al. 2015) or other bodies (such as Mercury). In particular, the mid-infrared (MIR) range is very sensitive to the silicate composition with features around 10 μm associated with the Si–O stretching modes, either anhydrous or hydrated.

Thus, we present here new ion irradiation experiments of several CCs to further explore their diverse spectral response to irradiation in the MIR range related to composition. We especially focus on the CM family, as it shows the largest variety of spectral behaviors—a very good case study to explore the composition factor and make predictions on SpWe at the surface of diverse asteroid types.

We also used several energies to study the role of the slow and fast solar wind (Urso et al. 2020), and we acquired spectra with two different setups to test how the observation geometry affects the identification of SpWe spectral effects in the MIR, as shown by Rubino et al. (2022) in the NIR.

2. Samples and Experiments

2.1. CC Selection

In order to enlarge the set of CCs investigated in previous studies, we choose the following CCs: the CK NWA5515-1498, the CR EET92159, and the CMs MET01070 and QUE97990. Even though a CK (ALH 85002) had been irradiated in a previous work using laser (Hiroi et al. 2013), the MIR spectra were not shown. No example of irradiation experiments on CRs is mentioned in the literature. Considering the CM samples, we selected the MET01070 meteorite because it is highly altered and rich in Mg phyllosilicates, while the QUE97990 meteorite is poorly altered and thus is Fe-richer (Rubin et al. 2007), to test the influence of variable chemical composition of the hydrated silicates in the spectral modifications upon irradiation.

In the context of sample return missions Hayabusa2 and OSIRIS-REx, we also irradiated a few meteorites that had been considered good analogs for Ryugu and Bennu (at the time we designed this experiment). Based on NIRS3 spectra (Kitazato et al. 2019), we selected the following meteorites: the shocked CM MET01072 and the partially dehydrated CI-like Y980115 (now considered CY, a petrologic group defined by Ikeda et al. 1992 and proposed to be a good analog to Ryugu; King et al. 2019), both of which showed reflectance spectra similar to Ryugu. In the same manner, we selected the CM MET00639 that was compared to Bennu's global OVIRS spectrum (Hamilton et al. 2019). We also irradiated a chip of the Almahata Sitta meteorite (Zolensky et al. 2010)—to be compared to Bennu, as they both show a large diversity of albedos/lithologies (Campins 2019)—referenced as a ureilite.

Finally, we used a large piece of CM Murchison that was broken into two separate pieces (after the sample preparation described in the previous section), which were irradiated at two different facilities (see Section 2.2).

Table 1 summarizes the samples and the experimental conditions.

2.2. Methods

Meteoritic samples were prepared according to different methods: some were in the form of pellets, and others were chips. Pellets were obtained similarly to previous studies (e.g., Hiroi et al. 2013; Lantz et al. 2017) by pressing powder with a typical grain size of $<150\,\mu$m. Chips were made from centimeter-sized samples with a flat surface and roughness controlled by a #400 polishing disk (Nakamura et al. 2019).

We favor flat surfaces to obtain uniform irradiation on the whole sample and to simplify the IR analysis performed through a 2D detector (see below).

We performed ion irradiation of the samples on the SIDONIE ion separator (JANNuS-SCALP platform of IJCLab, Orsay) within the INGMAR vacuum chamber (room temperature, $P \sim 10^{-7}$ mbar). We used He^+ at energies of 15, 20, or 40 keV and an ion fluence of 6×10^{16} ions cm^{-2} to be comparable with previous ion irradiation experiments dedicated to SpWe studies (Brunetto et al. 2014; Lantz et al. 2017; Rubino et al. 2020). We also irradiated one sample with 4 keV He^+ at ISAS/JAXA using the same ion flux of 10^{13} ions (s cm^2)$^{-1}$ as in Orsay and reaching the same final fluence of 6×10^{16} ions cm^{-2}. Thus, the conditions of the two experiments are the same, except for the energy, in order to study its role in modifying the meteorite spectra.

The MIR reflectance spectra (4000–800 cm^{-1}) presented in this paper were acquired ex situ with an Agilent Cary 670/620 microspectrometer equipped with a 128 × 128 pixel focal plane array (FPA) detector, installed at the SMIS beamline of the SOLEIL synchrotron (France). Spectra were acquired using the internal Globar source and with respect to a reference obtained on a gold plate. More details on this instrument can be found in Brunetto et al. (2018). It is important to note here the geometry of this measurement: a Schwarzschild objective (x15, numerical aperture 0.62, projected pixel size ~5.5 μm) was used to

Table 1
List of Meteorites (Name and Class) Irradiated for This Study

Meteorite Name	Class	Type	Sample Form	Energy (keV)	FTIR Setup
MET01070	CM	1	Pellet	15	Agilent w/ FPA
				40	
QUE97990	CM	2	Pellet	40	Agilent w/ FPA
MET01072	CM	2	Chip	20	Agilent w/ FPA
					Bruker Vertex
MET00639	CM	2	Pellet	20	Agilent w/ FPA
Murchison	CM	2	Chip	20	Agilent w/ FPA
			Chip	4	Agilent w/ FPA
					Bruker Vertex
Y980115	CY	1	Pellet	20	Agilent w/ FPA
			Chip	20	Agilent w/ FPA
					Bruker Vertex
NWA5515-1498	CK	4	Pellet	15	Agilent w/ FPA
				40	
EET92159	CR	2	Pellet	40	Agilent w/ FPA
Almahata Sitta	Ureilite	Anomalous	Chip	20	Agilent w/ FPA

Note. Sample preparation, energy, and IR setup used are also given. All samples were irradiated with the same ion fluence and flux. Petrologic type is from the Meteoritical Bulletin (https://www.lpi.usra.edu/meteor/).

illuminate the samples, and the same objective was used to collect the backscattered light and send it to the detector.

For most of the samples, we acquired maps (mosaics of several tiles, each sized ∼700 μm) before and after irradiation, allowing us to compare the same spatial region. We averaged large areas (mm^2 to cm^2, tens of thousands of spectra) to average out the small-scale heterogeneity of the samples and strictly discuss the irradiation effects (see Appendix C). Spectra were acquired with either 4 or 8 cm^{-1} spectral resolution and a number of scans of either 16 or 32.

A few samples were also measured at Tohoku University with an FTIR Bruker Vertex 70v (see Table 1 and Figure A1 and B1). In this case, the geometry was $i = 30°$, $e = 0°$, and a 30° phase angle, but a strict comparison (i.e., on the exact same area) before/after irradiation was not possible (sample preparation and measurement were done in Japan, but irradiation was performed in France). We thus extracted an average spectrum from a nonirradiated zone and another spectrum from an irradiated one.

3. Results

Figure 1 displays all the averaged MIR spectra before and after ion irradiation acquired with the Agilent/FPA instrument (see also Figure C1 for more details). We focus the study on the mineral component, especially the 10 μm region (1000 cm^{-1}), where the Reststrahlen bands are dominated by a strong surface scattering and are observed upward.

3.1. MIR Spectroscopy of Various CCs

The CK NWA5515-1498 (shown in Figure 1) looks like a typical CK spectrum or CV Allende with olivine features (main one at ∼890 cm^{-1}) dominating the spectrum (Beck et al. 2014).

The CR EET92159 is close to other CR2s with a clear influence of pyroxenes (major peak at ∼940 cm^{-1}) compared to a spectrum dominated by olivine (Beck et al. 2018).

The piece of ureilite from Almahata Sitta has very similar spectral features as the previous CR meteorite, inferring a pyroxene-rich sample. This is also in good agreement with previous MIR spectra of the Almahata Sitta meteorite (Hiroi et al. 2010).

Considering the five CMs studied here, they can be classified into two groups (see Figure 1): Murchison and QUE97990 on one side, with a broad feature centered around 955 cm^{-1}, and the MET samples, with a thinner band closer to 1000 cm^{-1}. The first group has a 10 μm feature that seems to mix several components (phyllosilicate around 1000 cm^{-1}, olivine around 870 cm^{-1}, and pyroxene in between), while the second group's spectra seem dominated by the hydrated minerals. This spectral classification is in agreement with the scale proposed by Howard et al. (2015), which evaluates the phyllosilicate fraction (PSF) thanks to modal mineralogy obtained by X-ray diffraction. MET01070 and MET01072 have a PSF of more than 90%, while Murchison and QUE97990 are closer to 70%–75%, meaning that the contribution of olivine is not negligible.

Finally, the CY Y980115 spectrum on the pellet is consistent with the one measured by King et al. (2015b): a peak close to 1000 cm^{-1} attributed to hydrated minerals and another one close to 890 cm^{-1} due to olivine contribution. Olivine in these CI-like meteorites has been found in a larger amount than in typical CIs (King et al. 2015a). The spectrum acquired on the chip is slightly different, with the peak of hydrated minerals not at the same position and a stronger olivine peak, consistent with the spectrum acquired by Matsuoka et al. (2022). This could be due to a different amount of both compounds between samples, especially here between the chip (rather heterogeneous) and the powder we used to make the pellet.

3.2. Ion Irradiation Spectral Effects

We focus now on the spectra (Figure 1) after ion irradiation as a simulation of the SpWe solar wind component.

The CK NWA5515-1498 was irradiated with 15 and 40 keV He^+: both spectra show a spectral shift of the whole 10 μm feature toward longer wavelengths, with the higher energy producing a bigger shift (∼16 cm^{-1}), almost twice as large as in the low-energy experiment. There is a shoulder in the left part of the band (marked with a star in Figure 1) before irradiation, which disappears after. Looking back at the

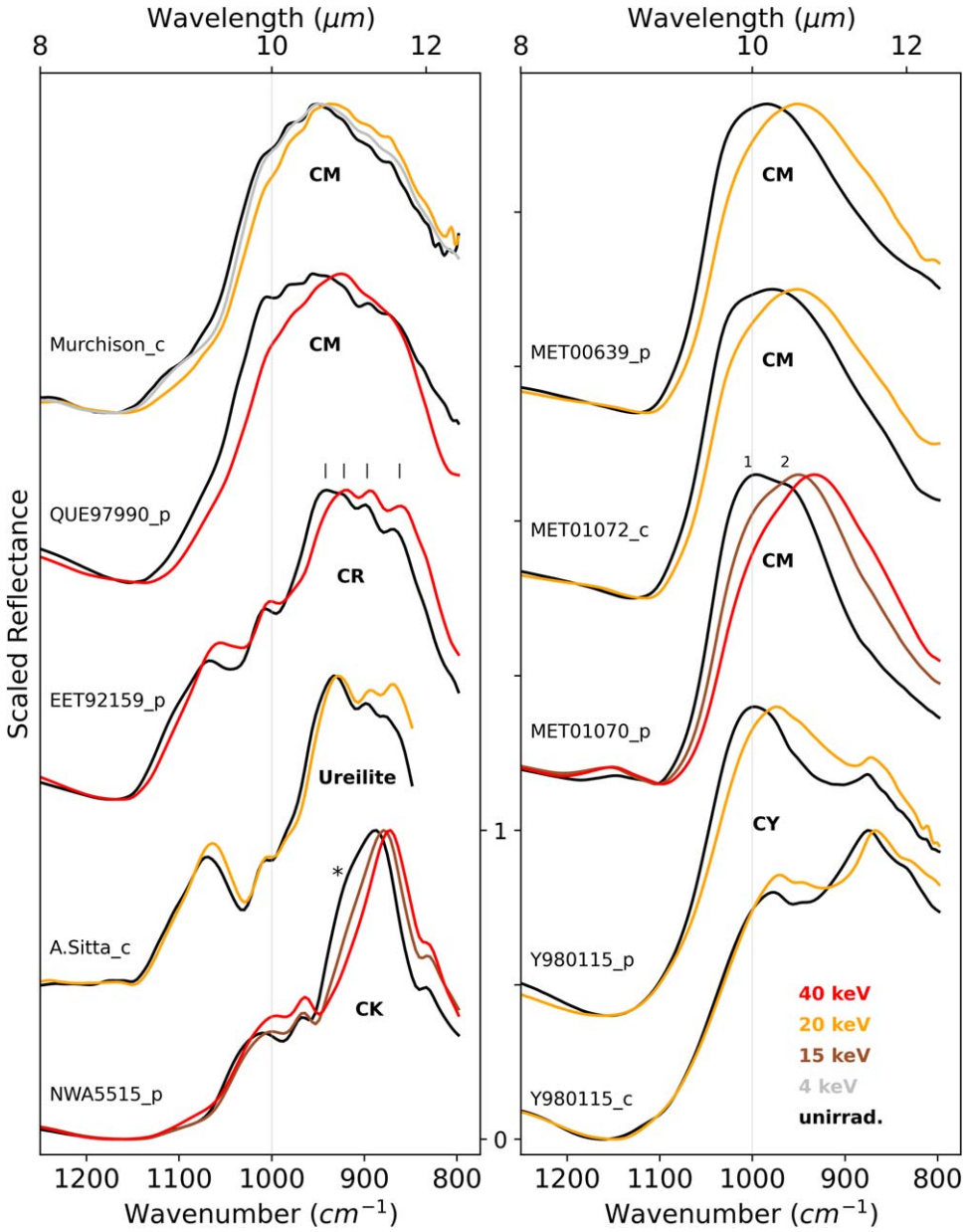

Figure 1. MIR confocal reflectance spectra of the meteorites. Spectra were acquired at SOLEIL (France) with the Agilent/FPA instrument (imaging) and averaged on a large area of the samples. In the left column (no or less hydrous compounds), from top to bottom: CM Murchison, CM QUE97990, CR EET92159, a ureilite piece of Almahata Sitta, and CK NWA5515-1498. In the right column (more hydrated minerals), from top to bottom: CM MET00639, CM MET01072, CM MET01070, and two different samples of CY Y980115. Sample names are indexed with c for chip and p for pellet. Nonirradiated area spectra are in black, while irradiated ones are in color: 4 keV in gray, 15 keV in brown, 20 keV in yellow, and 40 keV in red. Spectra are scaled to unity at the strongest peak to facilitate the comparison and are shifted along the *y*-axis for clarity. The marks on the CK, CR, and CM MET01070 spectra are discussed in Section 3.2.

Lantz et al. (2017) experiment, such an effect was also present on CV/CO meteorites undergoing ion irradiation with the same experimental conditions.

The 20 keV irradiation of the ureilite does not lead to a strong shift, but one can notice a change of band relative intensities on the main features at 900 cm^{-1}: the secondary peaks on the right side become relatively stronger. A similar effect is also seen on the CR meteorite. While the main band before irradiation shows four peaks (marked by ticks in Figure 1), only three remain after 40 keV irradiation: the first one seems to have disappeared, leading to an artificial stronger shift of the band maximum.

The CM QUE97990 has a smoother band (less visible tiny peaks, probably related to amorphization) after the 40 keV irradiation, and the maximum is shifted. The smoothing effect after 20 keV irradiation on Murchison is not so obvious, but the spectral shift happens: it is smaller, though, consistent with a lower energy than on the previous CM. The 4 keV experiment leads to a tiny shift on the Murchison sample (see Figure B1).

The second group of CMs has a very interesting behavior after irradiation. It is especially striking on MET01070, where the band is made of two components (two peaks at ∼1000 and ∼950 cm^{-1}, marked with numbers 1 and 2, respectively): the left peak (maximum, #1) is vanishing under irradiation (we see the transition from virgin to 15 and 40 keV), while the right peak (#2) becomes stronger and is shifted. The combined effect produces a very strong shift of the band maximum (∼60 cm^{-1}). It has to be noted that the 15 keV experiment is

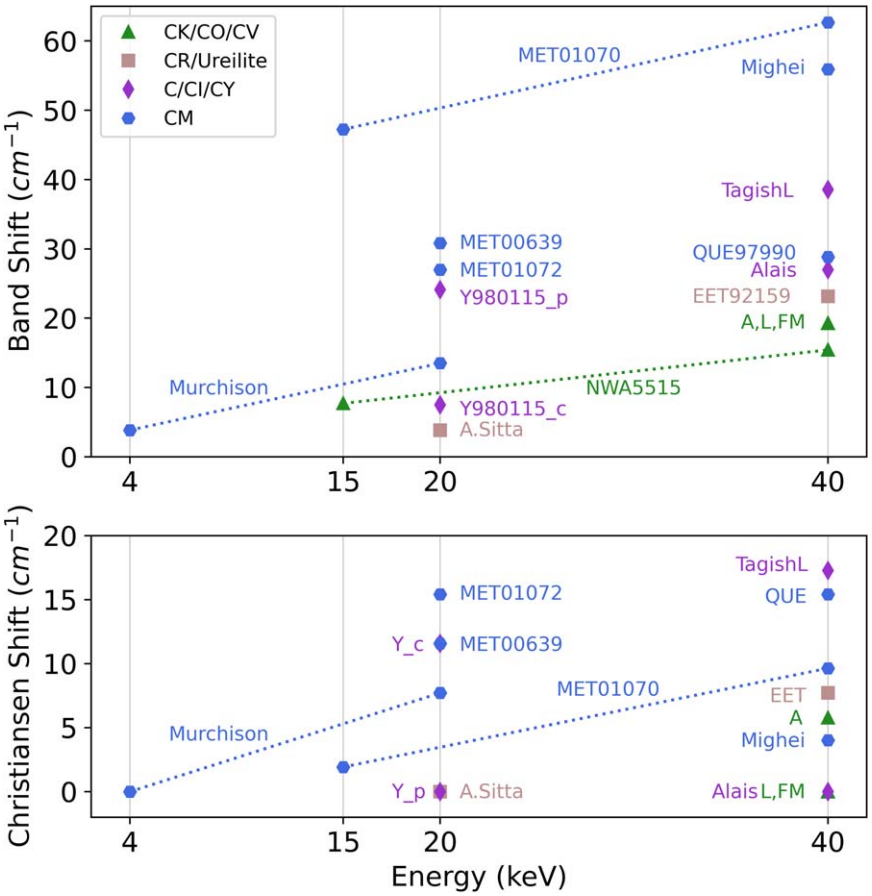

Figure 2. Shift values measured on all meteorites irradiated by our team using He^+ ions to simulate the SpWe solar wind component at different energies. The shift is determined by subtracting the position of the main band (maximum on the spectra; top panel) or Christiansen feature (bottom panel) before and after irradiation. Errors are within the symbol size. We grouped meteorites according to their classes: green triangles for anhydrous CCs, sand squares for pyroxene-rich samples, purple diamonds for the most hydrated meteorites, and blue hexagons for all CMs. We only considered the first peak for the Y980115 samples (both chip and pellet). The meteorites Allende, Lancé, and Frontier Mountain 95002 are abbreviated as "A, L, FM."

already very efficient to change the band shape and position (shift of $\sim$45 cm^{-1}). The two peaks of the band are also visible on the two other MET, but the spectra before irradiation are dominated by the right component with a shoulder on the left side (clearer in MET01072). There is quite a big shift ($\sim$30 cm^{-1}), even though the experiment was made at 20 keV.

The CY suffers a shift of the bands under 20 keV irradiation, with a stronger effect on the left one (located at $\sim$1000 cm^{-1}), corresponding to the main band of the second group of CMs.

We summarize in Figure 2 (top panel) the shift observed on the main Si–O bands (the strongest Reststrahlen bands) for each ion irradiation experiment at a final fluence of 6×10^{16} ions cm^{-2} performed so far by our team (this study and Lantz et al. 2017) on CCs to simulate the SpWe solar wind component. The shift value is determined as the subtraction between the maximum of the spectrum before and after irradiation. This is done without taking into account the potential effect of the peak intensity change. This means that the shift can be overestimated in some cases, as we are not comparing the same band peak before and after the irradiation. The philosophy behind this is that remote sensing data of asteroids are acquired with less good ($R \sim$ a few hundred at maximum) resolution than what can be done in the laboratory ($R \sim$ several thousand) and might not be sensitive to each peak we see here. We choose to perform the search of the band maximum in a way to realistically mimic what can be done on asteroid data.

On this plot, one can see that samples enriched with hydrated compounds (CI/CM) suffer a stronger spectral shift than the others (CV/CO/CK). This trend is even verified among the CMs that underwent different hydration stages. The comparison at 40 keV between the end-members MET01070 (highly altered) and QUE97990 (poorly altered) is striking: the MET shift is twice as big as on the QUE.

The effect on the ureilite at 20 keV is pretty low, following the anhydrous trend.

It is important to notice the unusual behavior of the Murchison meteorite, the typical CM, that is way less affected than the other CMs at the same energy of 20 keV. A previous experiment at 40 keV He^+ but with lower final fluences (1×10^{16} and 3×10^{16} ions cm^{-2}) did not produce a significant shift (less than 10 cm^{-1}; Lantz et al. 2015). By comparison, the shift on the CV Allende meteorite irradiated with 40 keV He+ at 3×10^{16} ions cm^{-2} produced a shift of $\sim$20 cm^{-1} (Brunetto et al. 2014). Similarly, the meteorite QUE97990 is less modified than Mighei and MET01070 at 40 keV. We could expect a spectral modification on Murchison similar to the one seen on QUE97990 with the same irradiation conditions (40 keV with He+ at 6×10^{16} ions cm^{-2}). The lower shift they suffer might be related to their petrologic type/initial

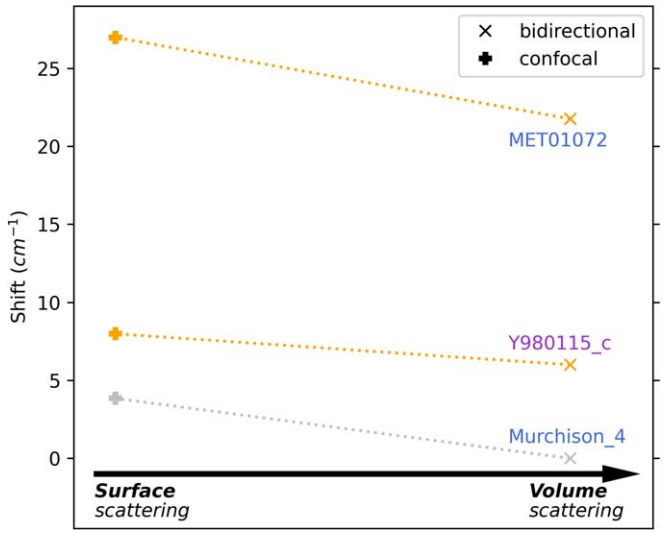

Figure 3. Comparison of shift values (determined on the main band in the MIR range) between data acquired at SOLEIL (microscope; plus signs) and at Tohoku University (bidirectional; crosses) on the same samples: CMs Murchison (irradiated at 4 keV; gray line) and MET01072 (20 keV; yellow), and CY Y980115 as a chip (20 keV; purple). Corresponding spectra are shown in Figure 1 (SOLEIL) and Figure A1 (Tohoku Univ.). The values presented here for the chip of Y980115 were obtained on the first peak around 980 cm^{-1}.

composition enriched in anhydrous compounds (inferred from the main MIR band shape and position in Figure 1).

For most meteorites, not only do the Reststrahlen bands shift after irradiation, but so do the Christiansen features (minima before the Si–O bands). We summarize in Figure 2 (bottom panel) the shifts measured also by a subtraction of the minimum when possible (the CK NWA5515 has several minima in this region before and after the irradiation, and thus it was not possible to determine the correct shift).

In general, the hydrated meteorites suffer a stronger shift (less than 20 cm^{-1}), but some olivine- or pyroxene-rich samples have quite a shift compared to others. For example, Allende makes a shift of ~8 cm^{-1}, while Lancé and Frontier Mountain do not move at all. This could be surprising, as they all have very similar spectra. But Allende's Christiansen feature is at 1120 cm^{-1}, while the two others are located at ~1150 cm^{-1}. The Christiansen feature position depends on the composition (Salisbury et al. 1991), and composition seems to play a role here too in the modification under ion irradiation.

3.3. Comparing Different Measurement Setups

As described in Section 2.2, we have acquired MIR spectra on some of the samples presented in Figure 1 with another setup (see Appendix A). We applied the same data analysis as before to determine the band position (search of the maximum) on spectra before and after the irradiation experiment. In Figure 3, we compare the results obtained by using the two spectrometers with different configurations (microscope at SOLEIL, bidirectional at Tohoku).

For the three samples, the spectral shift of the main band is larger with the microscope. The Murchison case at 4 keV is particularly interesting: while no significant change is observed with the bidirectional instrument, a shift is highlighted with the microscope (see Appendix B for a zoom on the considered spectra). It is also worth noting that the difference is less marked in the case of the CY chip dominated by anhydrous compounds. This strengthens the role played by initial composition on the SpWe spectral changes.

Having the opportunity to measure the samples with two different setups (bidirectional and confocal) allowed us to confirm in the MIR that geometry induces a bias on IR measurements for the detection of SpWe effects, as proposed by Rubino et al. (2022). As explained in this study, the incoming photons at small phase angles are ruled by surface scattering and probe the very first layers of the sample, the irradiated ones. On the contrary, a bigger phase angle would favor volume scattering (Adams & Filice 1967), and photons will probe both irradiated and virgin layers: irradiation effects can be diminished or hidden. In fact, phase angle is not the only factor. We confirmed here that the ratio between specular (enhanced with the microscope whose configuration favors the backscattering) and diffuse (the bidirectional instrument we used here rules out the specular component) reflection seems to play a role (near-specular configuration emphasizes the top layers) and should be taken into account when one looks for the SpWe spectral effects.

4. Discussion

4.1. Energy and Geometry Dependency

The use of different energies showed that a significant shift is achieved even with low energy (Figure 2). In particular, for the sample CM MET01070, the 15 keV irradiation produces a band shift equivalent to 75% of the total displacement reached at 40 keV (this number is 50% for the CK NWA5515). The increase in band shift with increasing energy can be explained by a competition between the ion and photon penetration depths. An SRIM (Ziegler et al. 2010) simulation gives a penetration depth for He^{+} ions in a target of approximate chondritic composition ($C_{0.2}Mg_{1.2}Fe_{0.8}SiO_4$, density of 2.2 g cm^{-3}) of about 160 nm and 390 nm at 15 keV and 40 keV, respectively. The depth probed by IR photons in a reflectance measurement of a solid target depends on the given wavelength, the molecular composition and optical properties of the target, and the observation geometry. In our back-scattering geometry, photons in the center of the silicate Reststrahlen bands probe probably less than 1 μm (Brunetto et al. 2020). We can thus interpret the increase in band shift as a function of the increasing energy and as a higher fraction of irradiated versus unirradiated layers probed by the Reststrahlen photons.

The fact that in the few cases explored here, the band shift does not seem to increase linearly with the ion energy suggests that for these samples, the penetration depth of ions at 40 keV is getting close to the depth probed by the IR photons of the main Reststrahlen band, implying that a saturation of the band shift should be observed if we increased the ion energy above 40 keV. However, the energy deposition (e.g., stopping power) is not uniform along the ion track. In addition, the relative amount of electronic versus nuclear stopping power generally increases with increasing energy, and the spectral variations probably correlate with the nuclear stopping power (Brunetto et al. 2014). All these factors can contribute to the nonlinear relationship between band shift and ion energy. A future characterization by transmission electron microscopy analyses of the irradiated layers shall clarify which is the main factor in determining the relationship between ion energy and band shift.

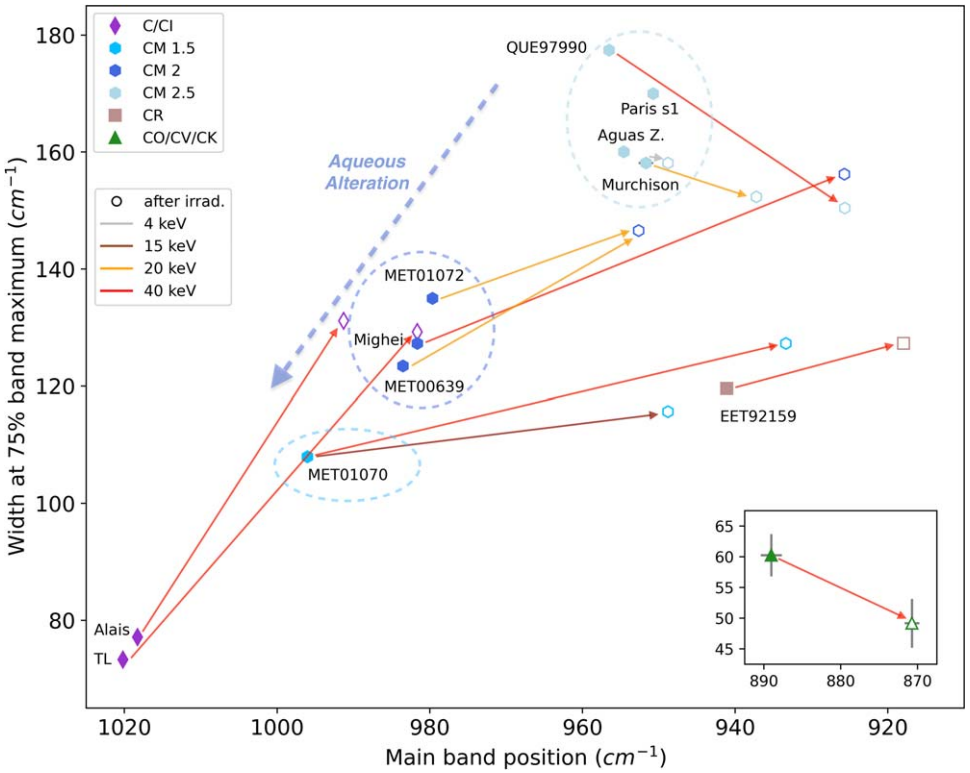

Figure 4. Evolution of the main band position vs. the width at 75% band maximum upon irradiation for all the studied chondrites. Filled symbols are before irradiation, and open ones are after, with color code as follows: 40 keV (red), 20 keV (yellow), 15 keV (brown), and 4 keV (gray). The inset plot is at the same scale as the main plot. We removed the CY sample, as its width is biased by the presence of two distinct bands, and the ureilite, as we do not have access to the value of the width at 75% height, preventing a straightforward comparison with the other samples. The dashed arrow defines a vector of aqueous alteration scheme among CMs (the three groups are circled), explained in Section 4.2.

We showed here that even relatively low energies can produce detectable spectral changes (mainly the shift of the main Si–O bands in the MIR) on surfaces exposed to SpWe processes. Since asteroids undergo modifications due to solar wind (dominated by ions at energies of about 1 keV amu^{-1}) and also more energetic particles (tens of keV to hundreds of MeV depending on their position in the solar system; Urso et al. 2020), one should expect to detect SpWe effects in the MIR on the different populations of atmosphereless bodies—including Mercury (Domingue et al. 2014), to be soon observed by the BepiColombo/ESA-JAXA mission (Benkhoff et al. 2021).

However, we have also shown that there is a competition between penetration depths of photons and ions, with a clear influence on the geometry of observation, similar to what we observed for the 2.7 μm band of irradiated phyllosilicates (Rubino et al. 2022). Thus, in order to maximize the detection of SpWe effects on a surface—both in the lab and remotely—one should favor a geometrical configuration for spectroscopic measurements as close as possible to specular reflection. This geometric dependency should also be taken into account when comparing results obtained by different teams on the IR spectral analysis of irradiated meteorites.

4.2. Composition Matters

We present in Figure 4 the distribution of the virgin and irradiated meteorites in a two-component-size space. We choose to use this kind of plot as it was previously shown to be a powerful tool to sort out measurements and distinguish meteorite types (e.g., Dionnet et al. 2022). Here we plot the width of the main Si–O band at 75% of its maximum (FWHM is not accessible due to the spectral limit of our detector) as a function of its position (around 1000 cm^{-1}).

We decided to further separate the CM meteorites into three groups (circled in Figure 4) according to their petrologic types, as three populations (roughly 1.5, 2, and 2.5) appear clearly separated before irradiation in this plot. Actually, this tendency defines a vector of aqueous alteration from the least altered QUE97990 to the most hydrated MET01070 (arrow in Figure 4). We emphasize the fact that most CMs are breccias with varying lithologies among one sample: it is difficult to classify each piece of meteorite we studied here according to previously published analyses. Thus, we classified them according to their petrologic type as given in the Meteoritical Bulletin, and we combined this scale with the ones by Rubin et al. (2007), Alexander et al. (2013), and Howard et al. (2015) to better fit with the parameter we are evaluating (main Si–O band position). Indeed, a good agreement between petrologic type and the Si–O band characteristics of CMs has been highlighted by Hanna et al. (2020).

We added two unirradiated CM samples previously studied with the same MIR instrument as for this analysis: a slice of Paris (Noun et al. 2019) and a piece of Aguas Zarcas (Dionnet et al. 2022). Both can be classified as type 2.5 and are unweathered. Their localization in the plot falls in the region of nonirradiated less aqueously altered samples, as expected.

First, Figure 4 confirms the general trend between the position before irradiation of the main Si–O band in the MIR range (here 9–12 μm) and the amount of hydrated minerals

(here depicted by the meteoritic classes and the petrologic types) as shown by McAdam et al. (2015).

The anhydrous chondrites (CV, CO, CK) clearly lie apart from the other classes despite the shift produced by irradiation on the hydrated meteorites (as already shown by Brunetto et al. 2020). This is important to note when one wants to evaluate the global composition of an object using remote sensing data. Those can often be noisy and cannot reveal a clear composition shape of the spectrum (phyllosilicate, olivine, pyroxene, etc.) but are mostly sensitive to peak position (for example, the Infrared Spectrograph instrument on Spitzer; Emery et al. 2006).

Considering the most hydrated chondrites (C/CI), the spectral shift of their spectra due to SpWe can hide them among nonirradiated CM-like surfaces.

Regarding the CMs, it is interesting to note that, for comparable energies, the final position of the band after the irradiation is almost the same no matter the initial position before irradiation. The samples MET01070, Mighei, and QUE97990 all start at different positions (spanning a range of about 50 cm^{-1} and revealing different degrees of aqueous alteration and/or relative ratio matrix/chondrules), but after irradiation at 40 keV, their main Si–O bands lie around 930 ± 5 cm^{-1}. We can extend this reasoning for the samples MET00639, MET01072, and MET01070 irradiated at 20 or 15 keV: for a similar irradiation dose, meteorites do not suffer the same effect (different shift values are observed), but they have a similar final position ($\sim$950 cm^{-1}) after irradiation. This trend would suggest that a maximum position is reached under irradiation effects, allowing one to put a limit on the range covered by the different CM-like surfaces and classify them from fresh to mature. Such saturation on SpWe had been previously observed in the case of the Allende meteorite, in particular with the far-infrared (FIR) bands (Brunetto et al. 2020).

Different trends appear when one looks at the bandwidth on the *y*-axis. Most samples have a larger band after irradiation (probably a sign of amorphization) with a stronger effect on the CIs, except for the CM2.5 samples, whose bandwidth decreases. This latter case is probably because of the higher number of anhydrous compounds within Murchison and QUE97990, as this trend is also seen on the CK/CO/CV samples. Such a plot highlights how composition effects are important when trying to decipher the SpWe processes. Highly aqueous altered samples (here CIs; Brearley 2006) suffer stronger amorphization, as the starting mineral is closer to a pure phyllosilicate (ordered crystal lattice). There is an intermediate group made of CM1.5–2 where some number of anhydrous compounds can be found (Howard et al. 2015) and the amorphization process would be less efficient. The CR sample follows this intermediate trend: either the hydrous component dominates the SpWe spectral answer, or the pyroxene component behaves differently from olivine under irradiation. Finally comes the last group (CM2.5 and CO/CV/CK), on which another process takes place to decrease the bandwidth. This could be due to the removal of a spectral component, as can be seen on the CK spectrum of Figure 1 (flagged with a star).

We note that after irradiation, the CM2.5 and CM2 groups fall in the same region of the plot, making them difficult to disentangle. When the time comes to plot remote sensing data on that kind of plot, an accumulation of points in this region would mean a matured population of CM-like asteroids, but the initial number of hydrated/anhydrous compounds could not be inferred. In some cases, coupling different spectral ranges might help to discriminate two different original compositions (e.g., the 2.7 μm band shape for CMs; Suttle et al. 2021); this is beyond the scope of this paper.

Because the additional CMs Paris and Aguas Zarcas perfectly fit the virgin CM2.5 group, one could infer that an irradiation experiment would place them at a higher band position but with thinner bandwidth.

Very few coordinated analyses investigating microstructural, chemical, and spectral changes in ion-irradiated samples exist. The studies of Murchison (Keller et al. 2015; Laczniak et al. 2021) and phyllosilicates (Rubino et al. 2024) all showed amorphization of the ion-affected regions and vesiculation, together with oxygen loss, Si enrichment, and Mg depletion. Rubino et al. (2024) specifically attributed the 10 μm bandwidth enlargement and position shift to the loss of the phyllosilicate texture (amorphization). More coordinated investigations are needed on various samples to decipher the complex SpWe behaviors seen on carbon-rich bodies.

5. Astrophysical Context

While highlighting in the laboratory several parameters playing a key role in the SpWe processes, it has to be wondered how to apply those findings to the astronomical observations. We showed (previous section) that bandwidth is a good tracer of SpWe varying effects related to the composition. However, this spectral parameter cannot always be used (limited spectral range or low signal-to-noise ratio). We tested in Figure 5 another parameter allowing us to separate the CC groups and thus hopefully the C-complex asteroid types: the difference in position between the Christiansen feature and the main band.

The major observation is that all the irradiated meteorites follow the same trend: the main band shifts toward longer wavelengths, and the distance with the Christiansen feature increases upon irradiation. The intensity of both displacements is a function of the energy we used: it is remarkable to notice that all vectors of SpWe (going from unirradiated to irradiated points) are almost parallel (summarized with a red arrow in Figure 5).

The anhydrous olivine-rich group (CV/CO/CK) is again well separated from the rest of the hydrated objects, with a distinction in the Christiansen position between CV and CO samples. The pyroxene-rich but hydrated CR sample lies between the anhydrous CCs and the mildly hydrated CMs. Then, the three CM populations are distinguished and aligned along a vector of aqueous alteration (blue arrow in Figure 5).

We note a caveat here concerning the CIs: the starting point on the *y*-axis might be overestimated due to a high concentration of sulfates formed under terrestrial alteration (as seen with Ryugu samples by Nakamura et al. 2023 and on the CI Orgueil by Dionnet et al. 2023). Indeed, such a component has a Christiansen feature at higher wavenumber than a pure phyllosilicate (it is located at 1165 cm^{-1} on the matrix of Orgueil and at 1250 cm^{-1} on a sulfate-rich zone), and the parameter we use here (difference with the main band position) is artificially increased. On the Alais data set, we excluded the spectra associated with clear sulfate signatures (only available before irradiation): the Reststrahlen band position was not affected, but the Christiansen feature decreased by about 40 cm^{-1}.

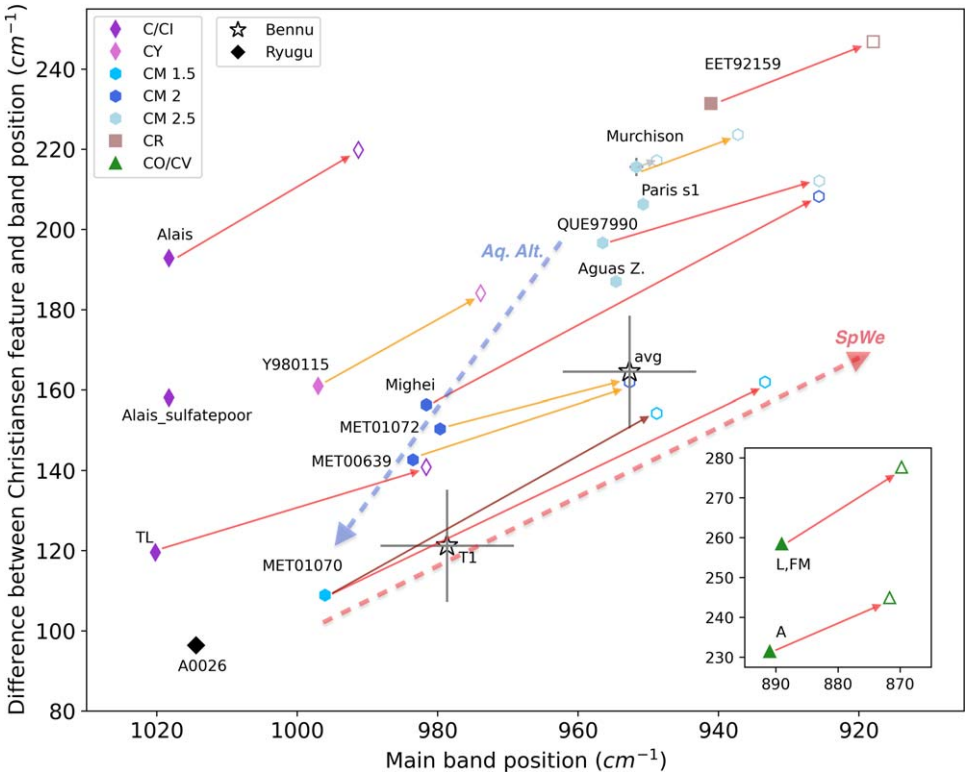

Figure 5. Evolution of the main band position vs. the difference between the Christiansen feature and main band position in the MIR upon irradiation. Filled symbols are before irradiation, and open ones are after, with the same color code as in Figure 4 (40 keV, red; 20 keV, yellow; 15 keV, brown; 4 keV, gray). The inset plot is at the same scale as the main plot. The meteorites Allende, Lancé, and Frontier Mountain 95002 are abbreviated as "A, L, FM." We added points for Ryugu (black diamond) and Bennu (star). Dashed arrows define the vectors of aqueous alteration (blue, as in Figure 4) and SpWe (red).

We highlight from this plot that aqueous alteration and SpWe processes follow different trends, as their "vectors" (going from CR EET92159 to CM1.5 MET01070 and from virgin to irradiated points; blue and red arrows, respectively) point toward two directions, allowing one to separate them when dealing with an unknown data set. Thus, when having a MIR observation of asteroids, one might be able to (i) determine its main type if unknown (hydrated or not and roughly which degree of aqueous alteration) and (ii) estimate if the surface suffered SpWe aging.

We added to this plot the available data for asteroids Ryugu and Bennu (targets of the sample return missions Hayabusa2/JAXA and OSIRIS-REx/NASA, respectively) to test some of our findings and/or predict their behavior under SpWe.

5.1. The Case of Ryugu

We included a lab spectrum of Ryugu sample A0026_pFIB01 (measured by the same IR setup as the irradiated chondrites presented in this study; Nakamura et al. 2023). The IR measurement was performed on a flat surface prepared as a pFIB section, thus representing a piece of Ryugu that was never exposed to SpWe. Virgin Ryugu lies in the domain of unirradiated C/CI, as already reported by the Preliminary Analysis Team—the difference in the Christiansen position is due to the presence of sulfates on CI meteorites.

By comparing with various laboratory experiments, Matsuoka et al. (2023) showed that SpWe by micrometeoroid bombardments promoting dehydration seems to be more effective than that by solar wind implantation. Another study by Hiroi et al. (2023) based on the shift of the 2.7 μm band (Lantz et al. 2017) showed that the uppermost surface of Ryugu suffered global-scale SpWe by solar wind. This shift has been reported among the sample collection (Le Pivert-Jolivet et al. 2023) and observed around the artificial crater on Ryugu (Kitazato et al. 2021). The preliminary analyses of Ryugu grains were able to detect several surface structures and features due to SpWe: melt splashes, amorphous and melt layers, bubbles, and Fe–Ni sulfide beads (Noguchi et al. 2023). These irradiated layers of Ryugu grains are ~100 nm in thickness, which could not be effective in producing large modifications of the VISNIR spectra because of the very dark surface and absorbing properties of Ryugu in the VISNIR (different from the case of Itokawa). In contrast, we show here the importance of MIR spectra to estimate solar wind implantation effects on asteroids. Unfortunately, there are no full MIR range spectroscopic remote sensing data acquired by Hayabusa2 (Hamm et al. 2022) to include a point for the mature Ryugu surface, but new studies on weathered Ryugu grains (Amano et al. 2023; Laforet et al. 2024) are showing spectral modifications of the 10 μm band that are in agreement with the ones shown in our experimental study.

However, we can try to predict where an irradiated Ryugu might fall in this plot: solar-wind-aged Ryugu (or at least this specific sample) would have spectral features following the SpWe vectors of Alais and Tagish Lake (here somewhere along the SpWe vector; red dashed line).

5.2. The Case of Bennu

Few remote sensing MIR spectra (instrument OTES) have been published by the OSIRIS-REx team. First, an average spectrum of Bennu (reported as avg on the plot) was acquired during the preliminary survey phase in 2018 December

(Hamilton et al. 2019). This spectrum should represent the overall surface of Bennu, thought to be matured by SpWe (Brunetto et al. 2020). Then, a study by Hamilton et al. (2021) revealed two end-member spectral types within the EQ3 survey: the T1 population having an asymmetric silicate stretching feature with a band position on the high wavenumber side ($\sim$987 cm^{-1})—compared to the global average spectrum–, and T2, which has a more symmetric shape with a band at $\sim$814 cm^{-1}. The T2 shape is attributable to the presence of deposits of fine particulates on Bennu. Because the T2 band position cannot be explained by SpWe (an enormous shift—almost 175 cm^{-1}—compared to what is seen in the lab, $\sim$60 cm^{-1}; Lantz et al. 2020), we consider here only T1. A comparison between OTES emissivity spectra and laboratory reflectance data can be made assuming Bennu's spectra do not exhibit strong volume scattering (Hamilton et al. 2019). A final spectrum represents materials deposited on the instrument optics postsampling Touch and Go (TAG) event (Lauretta et al. 2022). This last spectrum had been acquired in a different manner compared to the usual emissivity data of OTES and should be taken with caution: we do not include it on Figure 5.

In Figure 5, Bennu IR features fall in the area of CM chondrites. This is not surprising, as the main MIR band position at $\sim$10 μm is the typical feature of hydrated silicates. The alteration of Bennu is rather important, as large carbonate veins have been seen on orbital data (Kaplan et al. 2020). The band is pretty large, though, probably a sign of mineral mixture (typically a CM with type $\sim$2 following the scale we applied for this study). The band asymmetry would exclude a link with the less aqueous altered meteorites we present here (Murchison and QUE97990).

It is not straightforward to assume that the entire surface of Bennu underwent global SpWe (or during the same duration time) as episodes of particle ejection have been imaged by the OSIRIS-REx probe (Lauretta et al. 2019). This means that some surface gardening is taking place, probably allowing access to the unaltered subsurface. However, those virgin spots might be too small compared to the OTES footprint ($\sim$90 m; Hamilton et al. 2019) and not easily seen as isolated areas on orbital data. Thus, the T1 spectrum might not be representative of an unweathered surface but could be seen as a less matured surface than the average spectrum. Also, the average spectrum may include other processes than the SpWe (the presence of particulates, as already mentioned); thus, the spectral parameters we plot here might not be representative of the single contribution of SpWe on Bennu. We note that a recent combined analysis of NIR and FIR remote spectra seems to suggest phyllosilicate decomposition likely caused by SpWe or mild solar radiative heating (Hanna et al. 2024).

There is a clear trend between "fresher" T1 and "matured" average spectra, following the SpWe vector of Figure 5. From our study, we can infer that fresh Bennu shall lie close to the T1 region and even a bit more at the bottom left if we consider that T1 includes SpWe (see above). SpWe on Bennu would bring the irradiated point close to the average spectrum following the same SpWe vector as all the meteorites we studied.

Bennu's samples have just landed to Earth, and laboratory measurements will tell the ground truth of its SpWe history. The very first measurements seem to show that a fresh surface of Bennu is closer to the most hydrated CCs (Hamilton et al. 2024; Lauretta et al. 2024; Milliken et al. 2024). We shall highlight the fact that if Bennu is really associated with CMs, as most of them are breccias, several lithologies could be found among the returned samples. Thus, SpWe effects might differ depending on the studied sample composition.

6. Conclusion

We presented in this study a large set of CC MIR spectra to explore the SpWe effects under ion irradiation. We focused on the Reststrahlen bands, as those are indicative of the mineralogy, and numerous data in this spectral range are incoming thanks to the JWST. We extended the study by Lantz et al. (2017) to show that there is a systematic shift of the silicate bands that can be used as a reliable tool to remotely detect matured asteroid surfaces. Depending on the remote sensing data quality (the signal-to-noise ratio), one could classify asteroid MIR spectra into some sort of taxonomy (like what is done in the VISNIR; DeMeo et al. 2009; Mahlke et al. 2022) and evaluate the degree of SpWe/family age by looking at MIR parameters (e.g., Figures 4 and 5).

We showed that even lighter irradiation produces a spectral shift of the silicate bands in the MIR range, but the effects can be hidden to the observer if the spectrum is not acquired with favorable geometry, due to a competition effect between ion implantation depth and photon probe depth. Thus, it is important to take into account the geometry of the observation to ensure the measurement is sensitive to a thin irradiated layer. On orbital remote sensing data, it could be interesting to compare a region observed with two different geometries probing two depths to search for any significant difference related to SpWe.

By looking at different compositions, we highlighted different trends of SpWe spectral changes, and we found that hydrated asteroids' MIR features are more efficiently modified by SpWe processes. Furthermore, we emphasize the fact that SpWe analyses shall be performed on different kinds of samples to broaden the view of SpWe on primitive materials.

We plotted typical MIR features in two-component-size spaces to disentangle the different populations (with varying starting composition) and applied our findings to surmise the behavior of Ryugu and Bennu under ion irradiation. The in-depth analysis of Ryugu and Bennu samples on Earth will provide the ground truth of SpWe physical and chemical change on these objects that will help better understand remote sensing observations of C-type asteroids. This will also be a unique opportunity, as for Itokawa and the Moon before, to compare real SpWe features with what is currently simulated in the lab and to adjust the experiments.

Finally, let us note that the BepiColombo mission will survey Mercury's surface in early 2026 (Rothery et al. 2020). Currently, little is known about SpWe on Mercury, and the commonly used VISNIR parameters (albedo, slopes) might suffer the same weakness as for the asteroids: the spectral answer depends on the initial composition. The MERTIS instrument (Hiesinger et al. 2020) observations will then offer a good alternative to study SpWe in the MIR on Mercury.

Acknowledgments

We warmly thank the Vatican Observatory and P. Beck for providing us with the meteorite CK NWA5515 and CR EET97990 samples, respectively. We thank D. Ledu, C. O. Bacri, and P. Benoit-Lamaitrie for technical support on SIDONIE and INGMAR. INGMAR is a joint IAS-IJCLab facility funded by the P2IO LabEx (ANR-10-LABX-0038) in the framework Investissements d'Avenir (ANR-11-IDEX-

0003-01). The ex situ microspectroscopy measurements were supported by grants from Region Ile-de-France (DIM-ACAV) and SOLEIL. This work has been funded by the ANR project CLASSY (grant ANR-17-CE31-0004-02) of the French National Research Agency. C.L. and R.B. acknowledge the funding of the French National Space Agency (CNES). We thank Moe Matsuoka and an anonymous referee for their constructive reviews, which helped improve the manuscript.

Data Availability

Spectral data will be made available on the Database for AstrochemistrY and SpectroscopY at IAS-Orsay (DAYSY) database (https://www.sshade.eu/db/daysy/; Brunetto & Baklouti 2016) at the Solid Spectroscopy Hosting Architecture of Databases and Expertise (SSHADE) infrastructure (https://www.sshade.eu/; Schmitt et al. 2018). The SSHADE data is availabe at doi:10.26302/SSHADE/EXPERIMENT_ZED_20240701_01 (Lantz & Brunetto 2022).

Appendix A

We present in Figure A1 the measurements performed at Tohoku University with bidirectional geometry. These data are used in Figure 3. We overplotted the FPA data (dashed lines) for comparison (see Appendix B for Murchison).

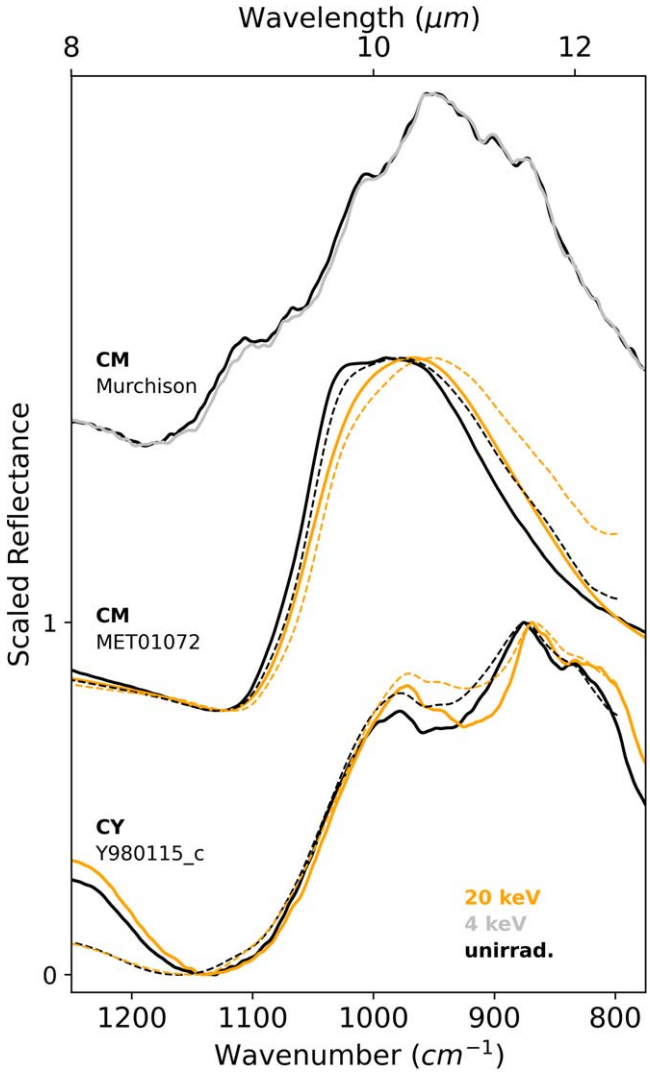

Figure A1. MIR bidirectional reflectance spectra of the meteorites CM Murchison (top), CM MET01072 (middle), and CY Y950115 as a chip (bottom) before (black) and after (colored lines) ion irradiation. Spectra are acquired at Tohoku University (Japan) with the Bruker Vertex instrument (solid lines) and at SOLEIL (France) with the Agilent/FPA instrument (dashed lines). Spectra are scaled to unity at the strongest peak to facilitate the comparison and are shifted along the *y*-axis for clarity.

Appendix B

We present in Figure B1 a zoom-in of the measurements acquired on the Murchison samples with the two different setups (microscope at SOLEIL and bidirectional at Tohoku). These data are presented in Figures 1 and A1, respectively. We remind the reader that these four spectra are not acquired at the same location on the sample.

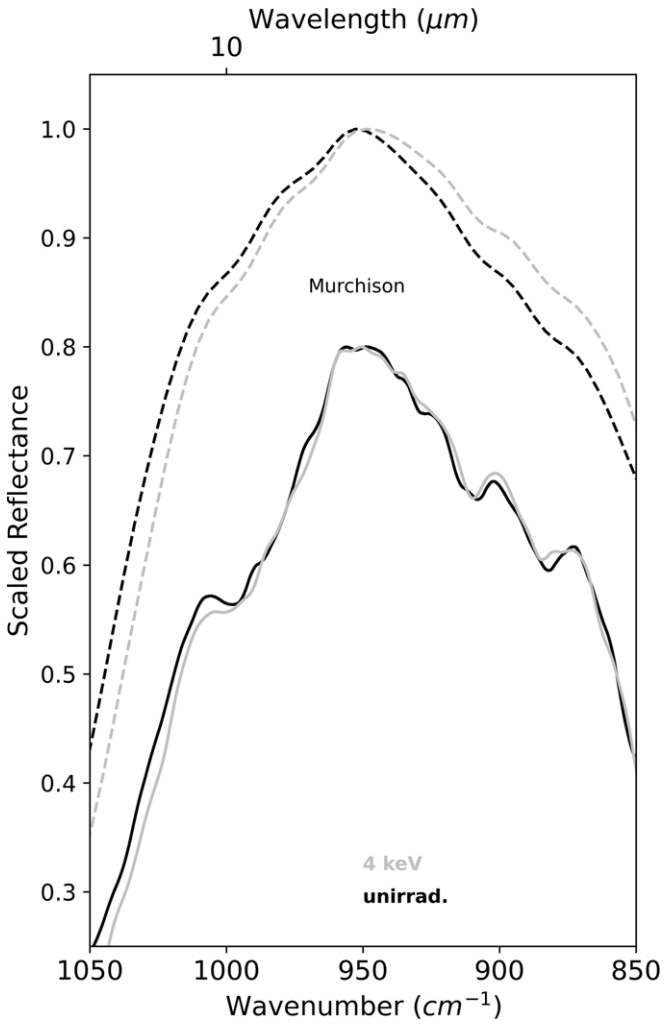

Figure B1. MIR confocal (dashed lines) and bidirectional (solid lines) reflectance spectra of the meteorite CM Murchison before (black) and after (gray) ion irradiation. Spectra are scaled to unity at the strongest peak to facilitate the comparison and are shifted along the *y*-axis for clarity.

Appendix C

The mapping ability tool of the MIR microspectrometer equipped with an FPA detector (at SOLEIL) was not fully exploited for this analysis, except to define the same areas on the sample before and after the ion irradiation experiment. In some cases, we irradiated half of a pellet with an ion energy (15 keV) and irradiated the other half with another energy (40 keV). To compare the two experiments, we had to make sure that the spectrum before irradiation was the same in both areas. We show in Figure C1 the example of the CK pellet on which three spectra were acquired in several zones and yet are identical. A similar observation is made on the CM pellet sample on which two different energies were also used.

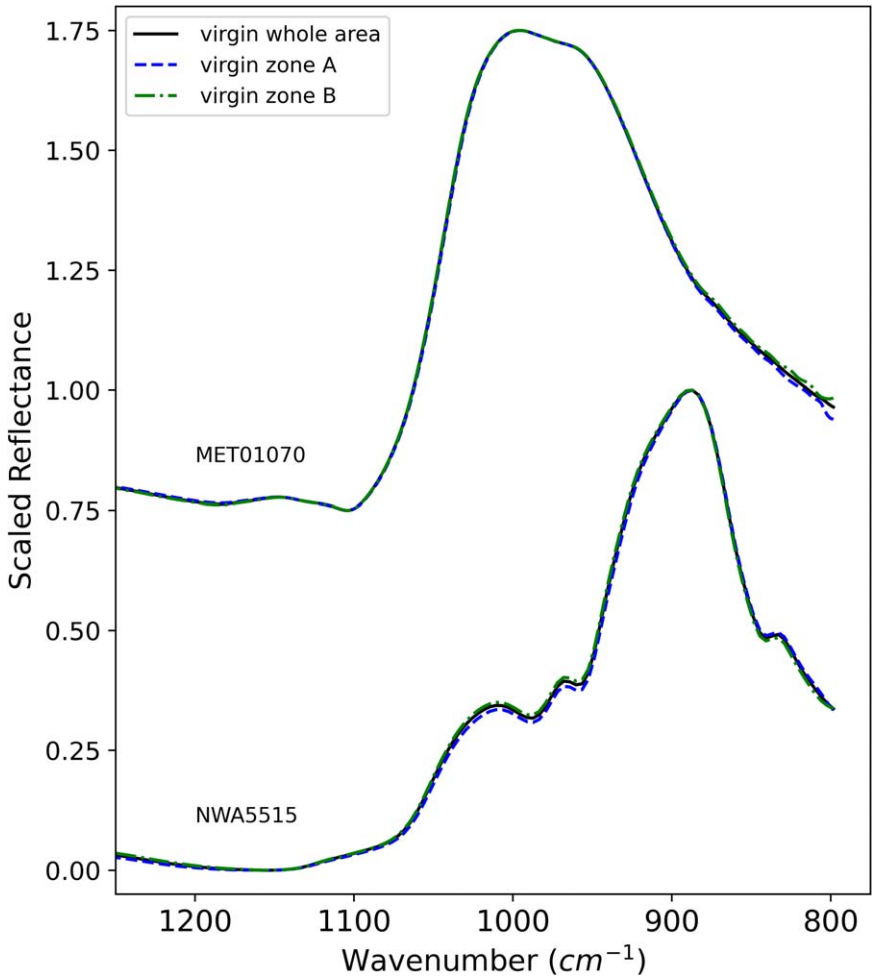

Figure C1. MIR confocal reflectance spectra of the meteorites CK NWA5515-1498 and CM MET01070 acquired on the pellet before ion irradiation exposure. The whole surface has been measured to produce a large area average spectrum (black). Two smaller areas (half pellet; blue and green lines) were also averaged to be compared afterward to the 15 and 40 keV irradiated zones. Spectra are scaled to unity at the strongest peak to facilitate the comparison and are shifted along the *y*-axis for clarity.

ORCID iDs

C. Lantz https://orcid.org/0000-0003-0974-4770
D. Baklouti https://orcid.org/0000-0002-2754-7829
R. Brunetto https://orcid.org/0000-0003-3001-9362
E. Henault https://orcid.org/0009-0001-3076-0073
Z. Djouadi https://orcid.org/0000-0001-5856-494X

References

Adams, J. B., & Filice, A. L. 1967, JGR, 72, 5705
Alexander, C. M. O. 'D., Howard, K. T., Bowden, R., & Fogel, M. L. 2013, GeCoA., 123, 244
Amano, K., Matsuoka, M., Nakamura, T., et al. 2023, SciA, 9, eadi3789
Beck, P., Garenne, A., Quirico, E., et al. 2014, Icar, 229, 263
Beck, P., Maturilli, A., Garenne, A., et al. 2018, Icar, 313, 124
Benkhoff, J., Murakami, G., Baumjohann, W., et al. 2021, SSRv, 217, 90
Bonal, L., Brunetto, R., Beck, P., et al. 2015, M&PS, 50, 1562
Brearley, A. J. 2006, in Meteorites and the Early Solar System, ed. D. S. Lauretta & H. Y. McSween, Jr (Tucson, AZ: Univ. Arizona Press), 584
Brunetto, R., & Baklouti, D. 2016, SSHADE/DAYSY: Database for AstrochemistrY and SpectroscopY at IAS-Orsay (OSUG Data Center), doi:10.26302/SSHADE/DAYSY
Brunetto, R., Lantz, C., Dionnet, Z., et al. 2018, P&SS, 158, 38
Brunetto, R., Lantz, C., Ledu, D., et al. 2014, Icar, 237, 278
Brunetto, R., Lantz, C., Nakamura, T., et al. 2020, Icar, 345, 113722
Brunetto, R., Loeffler, M. J., Nesvorný, D., Sasaki, S., & Strazzulla, G. 2015, in Asteroids IV, ed. P. Michel, F. E. DeMeo, & W. F. Bottke (Tucson, AZ: Univ. Arizona Press), 597
Campins, H. 2019, EPSC-DPS Joint Meeting, EPSC–DPS2019–1200
Clark, B. E., Hapke, B., Pieters, C., & Britt, D. 2002, in Asteroids III, ed. W. F. Bottke, Jr. et al. (Tucson, AZ: Univ. Arizona Press), 585
Clark, B. E., Lucey, P., Helfenstein, P., et al. 2001, M&PS, 36, 1617
DellaGiustina, D. N., Burke, K. N., Walsh, K. J., et al. 2020, Sci, 370, eabc3660
DeMeo, F. E., Binzel, R. P., Slivan, S. M., & Bus, S. J. 2009, Icar, 202, 160
DeMeo, F. E., & Carry, B. 2014, Natur, 505, 629
Dionnet, Z., Aléon-Toppani, A., Brunetto, R., et al. 2022, M&PS, 57, 965
Dionnet, Z., Rubino, S., Aléon-Toppani, A., et al. 2023, M&PS, 59, 1859
Domingue, D. L., Chapman, C. R., Killen, R. M., et al. 2014, SSRv, 181, 121
Emery, J. P., Cruikshank, D. P., & Van Cleve, J. 2006, Icar, 182, 496
Fornasier, S., Lantz, C., Perna, D., et al. 2016, Icar, 269, 1
Gillis-Davis, J. J., Lucey, P. G., Bradley, J. P., et al. 2017, Icar, 286, 1
Hamilton, V. E., Christensen, P. R., Kaplan, H. H., et al. 2021, A&A, 650, A120
Hamilton, V. E., Keller, L. P., Haenecour, P., et al. 2024, LPSC, 55, 1366
Hamilton, V. E., Simon, A. A., Christensen, P. R., et al. 2019, NatAs, 3, 332
Hamm, M., Grott, M., Senshu, H., et al. 2022, NatCo, 13, 364
Hanna, R. D., Hamilton, V. E., Haberle, C. W., et al. 2020, Icar, 336, 113760
Hanna, R. D., Hamilton, V. E., Haberle, C. H., et al. 2024, Icar, 408, 115809
Hiesinger, H., Helbert, J., Alemanno, G., et al. 2020, SSRv, 216, 110
Hiroi, T., Abe, A., Kitazato, K., et al. 2006, Natur, 443, 56
Hiroi, T., Jenniskens, P., Bishop, J. L., et al. 2010, M&PS, 45, 1836
Hiroi, T., Milliken, R. E., Robertson, K. M., et al. 2023, Icar, 406, 115755
Hiroi, T., Misu, S., & Nakamura, T. 2013, LPSC, 44, 1276

Howard, K. T., Alexander, C. M. O. 'D, Schrader, D. L., & Dyl, K. A. 2015, GeCoA, 149, 206
Ikeda, Y., Noguchi, T., & Kimura, M. 1992, in Proc. NIPR Symp. 5, Sixteenth Symp. on Antarctic Meteorites, ed. K. Yanai et al. (Tokyo: National Inst. of Polar Research), 136
Ishiguro, M., Hiroi, T., Tholen, D. J., et al. 2007, M&PS, 42, 1791
Kaluna, H. M., Ishii, H. A., Bradley, J. P., Gillis-Davis, J. J., & Lucey, P. G. 2017, Icar, 292, 245
Kaluna, M., Masiero, J. R., & Meech, K. J. 2016, Icar, 264, 62
Kaplan, H. H., Lauretta, D. S., Simon, A. A., et al. 2020, Sci, 370, eabc3557
Keller, L. P., Christoffersen, R., Dukes, C. A., Baragiola, R., & Rahman, Z. 2015, LPSC, 46, 1913
King, A. J., Bates, H. C., Krietsch, D., et al. 2019, ChEG, 79, 125531
King, A. J., Schofield, P. F., Howard, K. T., & Russell, S. S. 2015a, GeCoA, 165, 148
King, A. J., Solomon, J. R., Schofield, P. F., & Russell, S. S. 2015b, EP&S, 67, 198
Kitazato, K., Milliken, R. E., Iwata, I. T., et al. 2019, Sci, 364, 272
Kitazato, K., Milliken, R. E., Iwata, T., et al. 2021, NatAs, 5, 246
Laczniak, D. L., Thompson, M. S., Christoffersen, R., et al. 2021, Icar, 364, 114479
Laforet, S., Le Guillou, C., de la Peña, F., et al. 2024, ApJL, 963, L45
Lantz, C., & Brunetto, B. 2022, MIR Spectra of Carbonaceous Chondrites Irradiated by He^{+} Ions, SSHADE/DAYSY (OSUG Data Center), doi:10.26302/SSHADE/EXPERIMENT_ZED_20240701_01
Lantz, C., Brunetto, R., Barucci, M. A., et al. 2015, A&A, 577, A41
Lantz, C., Brunetto, R., Barucci, M. A., et al. 2017, Icar, 285, 43
Lantz, C., Clark, B. E., Barucci, M. A., & Lauretta, D. S. 2013, A&A, 554, A138
Lantz, C., Hamilton, V. E., Brunetto, R., et al. 2020, LPSC, 51, 1850
Lauretta, D. S., Adam, C. D., Allen, A. J., et al. 2022, Sci, 377, 285
Lauretta, D. S., Connoly, H. C., Jr., Aebersold, J. E., et al. 2024, M&PS in press
Lauretta, D. S., Hergenrother, C. W., Chesley, S. R., et al. 2019, Sci, 366, eaay3544
Lazzarin, M., Marchi, S., Moroz, L. V., et al. 2006, ApJ, 647, L179
Le Pivert-Jolivet, T., Brunetto, R., Pilorget, C., et al. 2023, NatAs, 7, 1445
Mahlke, M., Carry, B., & Mattei, P.-A. 2022, A&A, 665, A26
Matsuoka, M., Kagawa, E-i, Amano, K., et al. 2023, ComEE, 4, 335
Matsuoka, M., Nakamura, T., Hiroi, T., Okumura, S., & Sasaki, S. 2020, ApJL, 890, L23
Matsuoka, M., Nakamura, T., Kimura, Y., et al. 2015, Icar, 254, 135
Matsuoka, M., Nakamura, T., Miyajima, N., et al. 2022, GeCoA, 316, 150
McAdam, M. M., Sunshine, J. M., Howard, K. T., & McCoy, T. M. 2015, Icar, 245, 320
Milliken, R. E., Hiroi, T., Schultz, C. D., et al. 2024, LPSC, 55, 1573
Morota, T., Sugita, S., Cho, Y., et al. 2020, Sci, 368, 654
Nakamura, T., Lantz, C., Kobayashi, S., et al. 2019, Annual Meeting of The Meteoritical Soc., 82, 6211
Nakamura, T., Matsumoto, M., Amano, K., et al. 2023, Sci, 379, abn8671
Nakauchi, Y., Abe, M., Ohtake, M., et al. 2021, Icar, 355, 114140
Nesvorný, D., Jedicke, R., Whiteley, R. J., & Ivezić, Z. 2005, Icar, 173, 132
Noguchi, T., Kimura, M., Hashimoto, T., et al. 2014, M&PS, 49, 188
Noguchi, T., Matsumoto, T., Miyake, A., et al. 2023, NatAs, 7, 170
Noun, M., Baklouti, D., Brunetto, R., et al. 2019, Life, 9, 44
Noguchi, T., Nakamura, T., Kimura, M., et al. 2011, Sci, 333, 1121
Prince, B. S., Magnuson, M. P., Chaves, L. C., Thompson, M. S., & Loeffler, M. J. 2020, JGRE, 125, e06242
Rieke, G. H., Ressler, M. E., Morrison, J. E., et al. 2015, PASP, 127, 665
Riu, L., Pilorget, C., Milliken, R., et al. 2021, Icar, 357, 114253
Rothery, D. A., Massironi, M., Alemanno, G., et al. 2020, SSRv, 216, 66
Rubin, A. E., Trigo-Rodríguez, J. M., Huber, H., & Wasson, J. T. 2007, GeCoA, 71, 2361
Rubino, S., Lantz, C., Baklouti, D., et al. 2020, PSJ, 1, 61
Rubino, S., Leroux, H,, Lantz, C., et al. 2024, Icar, 415, 116070
Rubino, S., Potin, S., Lantz, C., et al. 2022, Icar, 376, 114887
Salisbury, J. W., D'Aria, D. M., & Jarosewich, E. 1991, Icar, 92, 280
Schmitt, B., Bollard, P., Albert, D., et al. 2018, SSHADE/SSHADE: Solid Spectroscopy Hosting Architecture of Databases and Expertise (OSUG Data Center), doi:10.26302/SSHADE
Sugita, S., Honda, R., Morota, T., et al. 2019, Sci, 364, eaaw0422
Suttle, M. D., King, A. J., Schofield, P. F., Bates, H., & Russell, S. S. 2021, GeCoA, 299, 219
Tatsumi, E., Sakatani, N., Riu, L., et al. 2021, NatCo, 12, 5837
Thompson, S., Loeffler, M. J., Morris, R. V., Keller, L. P., & Christoffersen, R. 2019, Icar, 319, 499
Thompson, M. S., Morris, R. V., Clemett, S. J., et al. 2020, Icar, 346, 113775
Trang, D., Thompson, M. S., Clark, B. E., et al. 2021, PSJ, 2, 68
Urso, R. G., Baklouti, D., Djouadi, Z., Pinilla-Alonso, N., & Brunetto, R. 2020, ApJL, 894, L3
Vernazza, P., Fulvio, D., Brunetto, R., et al. 2013, Icar, 225, 517
Zhang, P., Tai, K., Li, Y., et al. 2022, A&A, 659, A78
Ziegler, F., Ziegler, M. D., & Biersack, J. P. 2010, NIMPB, 268, 1818
Zolensky, M., Herrin, J., Mikouchi, T., et al. 2010, M&PS, 45, 1618